2019

Monte-Carlo Simulations of Near-infrared Light Propagation in the Adult Human Head

David J.F. Cohen

Monte-Carlo simulations of near-infrared light propagation in the adult human head

David J. F. Cohen

Supervisor: Mamadou Diop

March 27, 2019

University of Western Ontario

416 Medical Sciences Building

London, ON N6A 5C1

Submitted in partial fulfillment of the requirements for undergraduate thesis in the Department of Medical Biophysics

The format and style of this report adheres to the guidelines specified by the Department of Medical Biophysics

Abstract

It has been found that approximately 45% of all patients who undergo heart surgery suffer a lack of brain oxygenation at some point during the operation. Unfortunately, monitoring cerebral oxygen saturation non-invasively in adults during surgery is extremely difficult. While near-infrared spectroscopy (NIRS) can be used to monitor cerebral oxygenation in neonates, extending it to adults is challenging due to the increased thickness of the extra-cerebral layers in adult heads. Two potential NIRS methods for monitoring brain oxygen saturation in adults are continuous-wave (CW) and time-resolved (TR) NIRS.

The primary objective of this project was to investigate which of these two NIRS methods is the best suited for detecting changes in adult cerebral oxygen saturation. This was achieved by i) developing a robust methodology for the segmentation and mesh generation from 3D MRI images of an adult head, ii) simulating CW-NIRS and TR-NIRS light propagation in the generated head mesh, and iii) comparing the sensitivity of both NIRS signals to changes in cerebral oxygenation. More specifically, a volumetric mesh was generated from 3D MRI images which were segmented into 4 tissue-types, consisting of the skin, skull, cerebrospinal fluid, and brain tissue. Photon propagation was simulated in the mesh for wavelengths ranging from 650 nm to 947 nm, using brain oxygen saturation levels ranging from 40% to 70%. These *in silico* experiments were designed to mimic typical measurements from CW-NIRS and TR-NIRS devices and were analyzed to determine the effectiveness of each modality at monitoring brain oxygen saturation.

The greatest difference in the values for the CW-NIRS was found at 696 nm. From the 70% brain oxygenation to the 40%, there was a difference of approximately 3%. A 0.004% difference was found at the isosbestic point (798 nm). For the 696 nm wavelength in the TR-NIRS, there was a difference of approximately 56%, with a maximum difference of 72.6% at 657 nm. Similar to the CW-NIRS, TR-NIRS had a 0% difference at the isosbestic point of 798 nm. Additionally, the TR-NIRS was unaffected by source detector distance, while CW-NIRS signal improved with distance from the source.

We found that TR-NIRS is more sensitive to changes in brain oxygen saturation in adults than CW-NIRS. Thus, while CW-NIRS is effective in neonates, the extra-cerebral layers in adults are too thick to make it a viable option. These simulations also suggest that TR-NIRS will be more appropriate than CW-NIRS in monitoring cerebral oxygenation in adult cardiac surgery patients.

Table of Contents

List of Figures

List of Abbreviations

3D…….	Three-dimensional
CSF……..	Cerebrospinal fluid
CW……	Continuous-wave
MMC…….	Mesh-based Monte-Carlo
MRI……..	Magnetic Resonance Imaging
NIRS…….	Near-infrared spectroscopy
RTE……..	Radiative transport equation
TPSF…….	Temporal point-spread function
TR…….	Time-resolved

Introduction

Background

The brain requires a constant supply of oxygen for normal function. In order to supply the brain with the oxygen it needs, the heart needs to be constantly pumping oxygenated blood. However, this constant flow is often interrupted during cardiac surgery (Sun, Lindsay, Monsoon, Hill, & Corso, 2012). It has been found that approximately 45% of all patients who undergo heart surgery suffer a brain infarction at some point during the operation (Grogan, Stearns, & Hogue, 2009). As such, there is a need for intraoperative monitoring of cerebral oxygen levels during cardiac surgery in order to detect decreases in brain oxygenation and allow physicians to intervene. While systemic blood oxygenation correlates with global cerebral oxygenation, regions of the brain may temporarily have compromised blood flow. To better monitor cerebral oxygenation, it is best to use systemic blood oxygenation monitoring in conjunction with other neuromonitoring modalities (Oddo & Bösel, 2014). In recent years, neurophysiological monitors, transcranial Doppler ultrasound, and near-infrared spectroscopy (NIRS) have all been suggested for use in neuromonitoring during cardiac surgery (Kowalczyk, Bachar, & Liu, 2016). The most promising of these methods is the use of NIRS, as it is less susceptible to electoral noise than neurophysiological monitors and has lower levels of user variability than transcranial Doppler ultrasound (Kowalczyk, Bachar, & Liu, 2016). However, it should be noted that NIRS has limitations of its own. Currently, NIRS has difficulty detecting meaningful signals from adults due to the thickness of the adult skull. The primary objective of this study was to investigate the effectiveness of two NIRS modalities, continuous-wave (CW) and time-resolved (TR), to find which is better suited for monitoring brain oxygenation during adult cardiac surgery operations.

Near-infrared Spectroscopy

NIRS is a neuromonitoring technique that uses non-ionizing radiation in the form of near-infrared light to non-invasively probe the brain and directly perform tissue spectroscopy (Sood, McLaughlin, & Cortez, 2015). The range of wavelengths typically used in NIRS is known as the first optical window, ranging approximately from 650nm to 1300nm (Shi, Sordillo, Rodriguez-Contreras, & Alfano, 2016). Unlike X-rays, which travel along the line of sight between a source and detector, light within the optical window undergoes a large degree of scattering and absorption while traveling through biological media, which can make it difficult to predict how the light will behave in a given tissue. This unpredictability makes creating accurate models of how near-infrared light behaves in a complex and heterogeneous medium very challenging.

The movement of light through biological tissues is described by four major variables (Taddeucci, Martelli, Barilli, Ferrari, & Zaccanti, 1996). These variables are the scattering coefficient, absorption coefficient, anisotropic factor, and refractive index. The scattering coefficient is an experimentally derived value which describes the number of scattering events expected to occur per unit distance. The absorption coefficient is also experimentally derived and represents the number of absorption events expected to occur per unit distance. The anisotropic factor describes the probability that a photon will be scattered in the forward direction, with one being perfectly forward scattered, negative one being perfectly backwards scattered, and zero being isotropically scattered. The refractive index describes the reduction in the speed of light through a given medium when compared to the speed of light in a vacuum. These four variables all depend on the wavelength of light, as well as the chemical composition of the medium the light is traveling through. Furthermore, these four variables are all independent of each other, meaning

that all variables must be calculated individually for every wavelength and medium (Jacques, 2013).

CW-NIRS versus TR-NIRS. Two promising NIRS techniques are CW-NIRS and TR-NIRS. CW-NIRS uses a continuous beam of near-infrared light with a constant amplitude and frequency. In the context of cerebral monitoring, detectors placed on the surface of the head measure the intensity of the light that reach them, and the changes in intensity are related to changes in the chemical composition of the brain, allowing for the monitoring of cerebral oxygenation (Diop, Elliot, Tichauer, Lee, & St. Lawrence, 2009). While CW-NIRS is highly effective in monitoring neural activity and oxygenation in neonates and infants, it faces a major challenge in adults. In neonates, the extra-cerebral layers are typically less than 2 mm, rising to an average of 4 mm in children 3 years old (Li et al., 2015). In contrast, the extra-cerebral layers in adults can reach up to 10 mm on the forehead (Verdecchia et al., 2016). Since light scattering and absorption increase with tissue thickness, fewer photons reaching the detectors will have penetrated the brain in adults than in neonates, reducing the measured signal changes in brain oxygen saturation. As a result, CW-NIRS is not as effective at monitoring adult cerebral oxygenation with probes positioned on the scalp, which is necessary for non-invasive cerebral monitoring. However, it should still be possible to monitor adult cerebral oxygenation using CW-NIRS.

Instead of a continuous beam, TR-NIRS uses short pulses of near-infrared light, typically only a few picoseconds in duration. The detectors used in TR-NIRS are highly sensitive to rapid changes in intensity, allowing for the creation of a temporal point spread function (TPSF). The TPSF is a measure of the intensity of the light reaching the detector as a function of time and can be used to estimate the optical properties of the tissue. In general, TR-NIRS is expected to be more

sensitive to changes in deep tissue but is more expensive to implement than CW-NIRS (Kienle & Patterson, 1997).

Objectives

The objectives of this project were three-fold. Our first aim was to develop a robust methodology for the segmentation and volumetric mesh generation from Magnetic Resonance Images (MRIs) in order to create realistic geometries for simulating near-infrared light propagation in the adult head. Second, we wanted to develop a simple method for easy and accurate modelling of the propagation of light in complex and heterogeneous geometries. The final objective was to investigate the effect of varying the oxygen saturation in the brain on the signal typically measured by the NIRS detectors in order to determine which of the two NIRS methods (i.e., CW or TR) is more suitable for monitoring cerebral oxygenation in adults.

Image Segmentation

In order to create an accurate geometric model, an MRI of a human adult head was segmented in 3DSlicer. The head was segmented into four tissue types, consisting of scalp, skull, cerebrospinal fluid (CSF), and brain. Once the head had been segmented, the segmentation was imported into MATLAB, where the Iso2Mesh toolbox was used to create a three-dimensional (3D) volumetric mesh (The MathWorks, Inc, 2018; Fang & Boas, 2009).

Photon Simulation

The radiative transport equation (RTE) (Machida, 2017) is the most accurate theoretical framework for modeling light propagation in tissue. Here we used a stochastic implementation of the RTE based on Monte-Carlo simulation of light transport in tissue. More specifically, we used the custom MATLAB toolbox Mesh-based Monte-Carlo (MMC) (Chen, Fang, & Intes, 2012). MMC simulations can accommodate complex heterogeneous geometries with varying tissue

optical properties. This allows for simulation of near-infrared light in models based on the real anatomical geometry and optical properties of the subject.

Theory

Simulating Brain Oxygen Saturation

NIRS is a tissue spectroscopy technique that can be used to measure the chemical composition of tissue. Thus, it is possible to simulate different levels of brain oxygenation by altering the chemical composition of brain tissue and accounting for how it would change with oxygen saturation. The major brain tissue chromophores within the wavelengths of the 1st optical window (i.e., 650-1000nm) are water, deoxyhemoglobin, and oxyhemoglobin. The rest of the chromophores in the brain contribute very little to overall light absorption, and thus they can be ignored in simulations (Johansson, 2010). Since the concentration of water in the brain is unaffected by the level of tissue oxygenation, the contribution of water to the absorption coefficient remains constant as oxygen saturation varies. While oxy- and deoxyhemoglobin vary due to the oxygen saturation, the total amount of hemoglobin can also be treated as constant. Thus, the oxygen saturation can be used to set what percent of the total hemoglobin is in the oxyhemoglobin form versus the deoxyhemoglobin form. With the known concentrations of the water, oxyhemoglobin, and deoxyhemoglobin, it is possible to calculate the absorption spectrum of the brain for various oxygen levels using Equation 1:

$$\mu_{a_{Brain}} = C_{Water} * \mu_{a_{Water}} + C_{Hbt} * (1 - SO_2) * \varepsilon_{\mathrm{Hb}} + C_{Hbt} * SO_2 * \varepsilon_{\mathrm{HbO2}} \quad (1)$$

In Equation 1, $\mu_{a_{Brain}}$ is the absorption coefficient of the brain, C_{Water} is the concentration of water in the brain, $\mu_{a_{Water}}$ is the absorption coefficient of water, C_{Hbt} is the concentration of total hemoglobin, SO_2 is the oxygen saturation of the brain, ε_{Hb} is the extinction coefficient of

deoxyhemoglobin, and ε_{HbO2} is the extinction coefficient of oxyhemoglobin. Equation 1 was used to model various oxygen levels in the brain.

Methods

Image Segmentation

An MRI of an adult male head was imported into 3DSlicer as a DICOM volume ("3DSlicer", 2019; Kikinis, Pieper, & Vosburgh, 2014; Fedorov *et al.*, 2012; Pieper, Lorensen, Schroeder, & Kikinis, 2006; Pieper, Halle, & Kikinis, 2004; Gering *et al.*, 2001; Gering *et al.*, 1999). Using thresholding, the head was isolated from the background. This also served to remove any signal that was not within the head of the subject, making it easier for later steps in the segmentation. Using further thresholding, the skin, skull, brain tissue, and CSF were roughly separated from each other and placed into their own segmentation layers.

In the skin layer, the *erase* tool was used to remove the eyes, and then a combination of the *erase* and *paint* tools were used to refine the definition of the skin to better correspond with the MRI images. The smoothing tool was then applied on the median setting to remove any minor points of noise or holes along the surface of the tissue. Thereafter, the *islands* tool was used to remove all pieces in the segmentation that were not connected to the main body segmentation structure, as those were not meant to be part of the skin segmentation. The *erase* tool was finally used once again to further refine the skin to the MRI data.

A similar process was repeated on the bone segmentation. The *erase* and *paint* tools were used to refine the segmentation, before using the *smoothing* tool on the median setting. The *islands* tool was used to manually remove pieces of segmentation that were judged to not be part of the bone. To ensure the skin and skull segmentations did not overlap, the skull segmentation was subtracted from the skin segmentation.

Thresholding was found to be ineffective for the CSF and brain tissue. In order to segment the brain tissue, the *level tracing* tool was used to manually outline the brain tissue in roughly 50% of the images in the MRI volume. The *draw* and *paint* tools were then used to refine the level traced segmentations, before the *grow from seeds* tool was applied to segment the other 50% of the images. It was found that when less than 50% of the images were segmented, the *grow from seeds* tool was ineffective. When a significant amount of the brain was properly segmented, the *grow from seeds* tool effectively segmented the remainder of the brain from the CSF. The *erase* and *paint* tools were then used to refine the segmentation.

The segmentation of the CSF was completed by creating a segmentation of the whole head, and then subtracting the skin, skull, and brain segmentations. Since the CSF layer has very little impact on NIRS simulations due to its extremely low absorption and scattering, it was judged that segmenting it using this method was sufficient.

The completed segmentations were exported into individual TIF files. The files were all exported with the same axis scale as the reference MRI image, which allowed for the uniform spacing in all axis dimensions in the file. The voxels in the TIF files were all 1 mm^3, which simplified mesh generation as we did not have to worry about scaling one dimension greater than another.

Mesh Generation

The TIF segmentation files were imported into MATLAB, where they were combined into a single image. The skin was assigned element property 1, the skull element property 2, the CSF element property 3, and the brain element property 4. All points in the image that were not assigned tissue values were assigned the value 0, which represented air. By combining the segmentations

into a single image in MATLAB instead of doing so before exporting them in 3DSlicer, we were able to maintain the distinct regions following mesh generation.

Using the custom toolbox Iso2Mesh, a 3D volumetric mesh was generated based on the combined image segmentation (Fang & Boas, 2009). A maximum element volume was set to 10 mm^3. The outputs of the mesh generation function are three arrays, containing the node list, face list, and element list. The nodes list is a list of all vertex coordinates in the mesh, the face list contains a list of the nodes the surface elements connect, and the element list contains the IDs of what nodes an element connects, as well as the element ID for that element. The element ID corresponds to the element property that we had assigned to the equivalent location in the combined image in the previous step.

Photon Simulation

Optical properties. Optical properties were assigned to each tissue type using published literature values. The values assigned can be found in Figure 1. Figure 1A shows the absorption coefficients of skin, skull, and CSF. Since varying the levels of brain oxygen saturation has no effect on the extra-cerebral layers, they were assigned static values that only varied with wavelength. For the brain, the absorption coefficients for various oxygen levels were computed using Equation 1 and the values for the absorption coefficient of water, and the extinction coefficients of oxy- and deoxyhemoglobin (Matcher et al., 1995). The computed brain absorption coefficient values can be seen in Figure 1B. For the simulations, a brain water concentration of 80% and a total hemoglobin concentration of 55 μmol/L were used (Auger et al., 2016). Using an initial oxygen saturation of 70%, the absorption coefficients for wavelengths ranging from 650nm to 947nm were calculated and assigned to the brain tissues.

The scattering coefficients of the skin, skull, CSF, and brain tissue were assigned the values shown in Figure 1C (Jacques, 2013). Since CSF is approximately 99% water, its scattering coefficient is extremely small and was assigned a value of 0.001 mm^{-1} (Jacques, 2013). The anisotropy factor was assigned values of 0.85, 0.85, 0.8, and 0.8 for the skin, skull, CSF, and brain tissue, respectively. Since the anisotropic factor does not change significantly with wavelength over the spectral range of the simulations, we assigned a single anisotropy value to each tissue (Jacques, 2013).

The refractive indexes for the skin, skull, and brain tissue were all set 1.4, and the refractive index for the CSF was set to 1.33. As with the anisotropic factor, the refractive indexes are almost wavelength independent over the spectral range of interest (Jacques, 2013).

Source and detector placement. In all the simulations, the source and detectors placements were the same. The source was placed in the middle of the forehead approximately 50 mm above the nose. Starting at 10 mm from the source towards the right side of the mesh, detectors were placed approximately every 5 mm to a maximum of 30 mm (see Figure 2). The placement of the detectors accounted for the curvature of the forehead and the detectors' radius were set to 1.5 mm to match a typical experimental scenario.

Following the placement of the detectors, nodes were added into the mesh at locations corresponding to each of the detectors. The volumetric mesh was then re-meshed to adapt the elements and faces to incorporate the new nodes.

Simulation parameters. The initial set of simulations were run using a single simulation with 10 million photons per wavelength with a brain oxygen saturation of 70%. The source direction was chosen to be directly in the negative Y direction, which was directly from the source placement on the forehead to the back of the head. The units of the mesh axes were set to 1 mm,

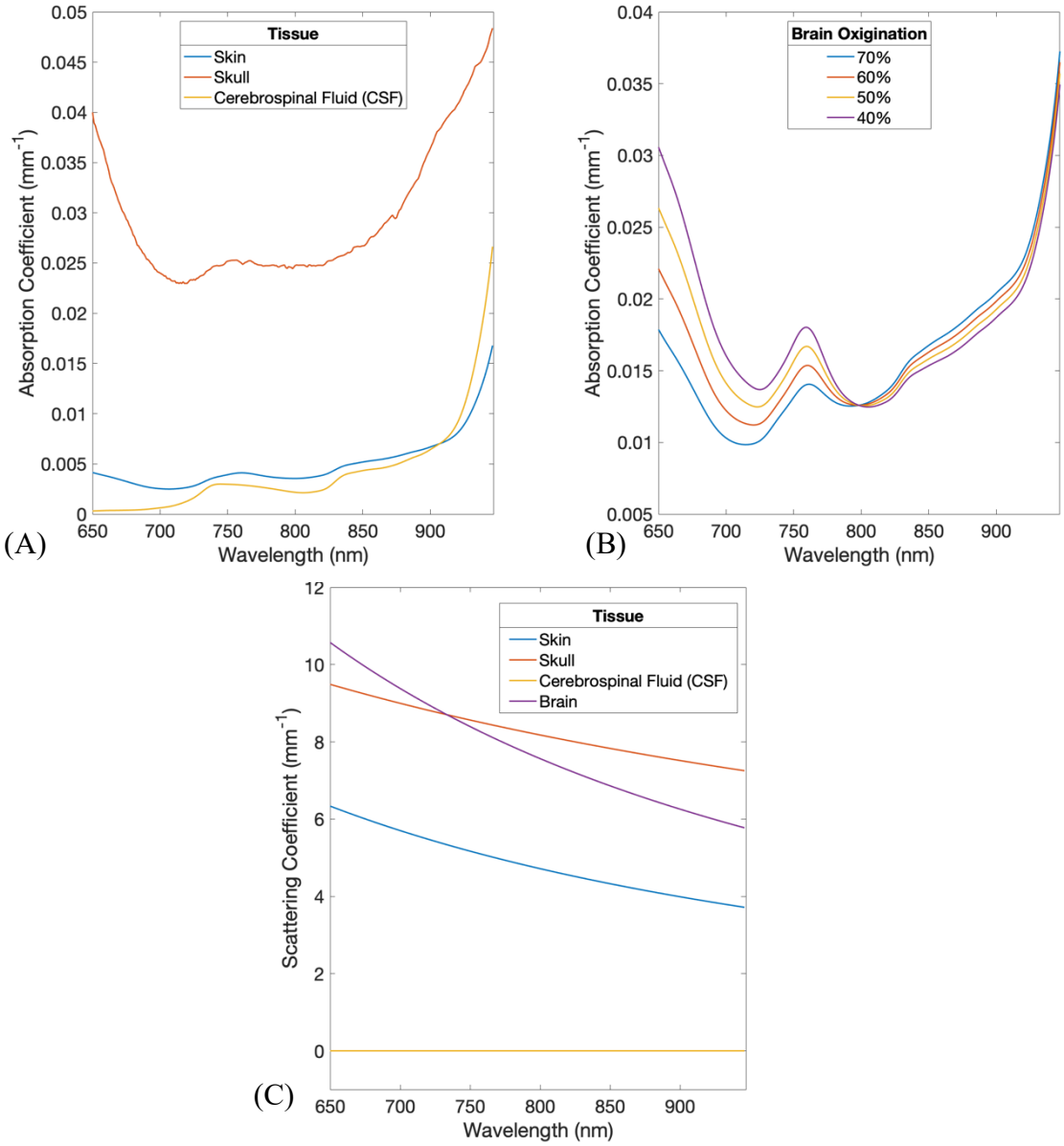

Figure 1. The absorption and scattering coefficients of the skin, skull, CSF, and brain tissue for wavelengths ranging from 650 nm to 947 nm. (A) The absorption coefficients of skin, skull, and CSF. These values do not change with oxygen saturation. (B) The calculated absorption coefficients of brain tissues for varying brain oxygen saturation levels. The hemoglobin isosbestic point is at approximately 798 nm. (C) The scattering coefficients for skin, skull, CSF, and brain; that of CSF is equal to 0.001 mm^{-1} for all wavelengths.

matching the units in the segmentation images which were used to construct the image. The simulations used a delta function to release the photons, resulting in all 10 million photons being released simultaneously at time equal to 0. The source of the photons was a laser of point thickness. The output type was set to fluence, which is the number of photons that pass through an element at each timepoint. The duration of the simulated time for each simulation was set to 5 ns, with the fluence being recorded and reset every 16 ps. The 5 ns duration was chosen as no signal was detected after that length of time in previous simulations, and 16 ps was chosen as it corresponds to the approximate Nyquist rate of the NIRS system used in our lab. In order to reduce computational time, the element volumes were pre-calculated, and inputted into MMC with the rest of the parameters.

To decrease the amount of noise in the simulations, ten simulations were completed with varying seed numbers and then averaged. The number of photons used in each simulation was decreased from 10 million photons to 1 million photons. This was done to maintain the same number of total photons being used when compared to the initial simulations. The 70% brain oxygen saturation simulations were then run again with these new parameters. The fluence at the detector nodes and the information of the detected photons were recorded.

Once the results of the 70% brain oxygen saturation simulations were complete, simulations were run with the oxygen saturations set to 60%, 50%, and 40%. After each oxygen saturation, the detector fluence and the information of the photons which reached the detectors were recorded.

Data Analysis

CW-NIRS. For each set of oxygen saturation simulations, the total fluence at each of the detectors were computed, then averaged to a single value for each wavelength to reduce the noise

inherent to the stochastic nature of the Monte-Carlo experiments. The total fluence for all wavelengths were plotted for each saturation level for all the source-detector distances.

The differences between the output of each of the saturation levels was additionally calculated against the 70% brain oxygen saturation. To compute the percent difference between the 70% brain oxygenation and the other saturation levels, Equation 2 was used:

$$\%Diff = \frac{(F_{70} - F_{Other})}{F_{70}} * 100\% \quad (2)$$

In Equation 2, $\%Diff$ is the percent difference, F_{70} is the fluence from the 70% brain oxygen saturation, and F_{Other} is the fluence from the other brain oxygen saturation level. The results were plotted for each source-detector distance.

TR-NIRS. In order to compare TR-NIRS with CW-NIRS, every oxygen saturation simulation set was once again loaded into MATLAB. The total fluence from 2 ns to 4 ns at every detector in each simulation were summed and then averaged to a single value per wavelength for each oxygen saturation. The 2 ns to 4 ns second photons were used as they represent late arriving photons, which have a higher probability of probing the brain. In contrast, CW-NIRS is heavily weighted towards early arriving photons, those arriving before 2 ns, which have mainly probed the extracerebral layers. The results of the varying oxygen saturation levels were plotted against each other for every source-detector distance. Equation 2 was used once again to compare the 70% oxygenation values with each of the other oxygen saturation levels.

Absorption coefficients were recovered from the TR-NIRS data using Equation 3:

$$\mu_a = \frac{m*c}{n} \quad (3)$$

In Equation 3, m is the slope of the natural logarithm of the TPSF between 2ns and 4ns for each wavelength of every oxygen saturation, c is the speed of light in a vacuum, and n is the refractive

index of the medium. The results of Equation 3 were plotted against each other, and visually compared with the inputted absorption coefficients of the brain.

Results

Brain Absorption Coefficient

The calculated absorption coefficients for the brain are shown in Figure 1B for the oxygen saturation levels of 40%, 50%, 60%, and 70%. The isosbestic point, the point where the absorption coefficients of oxygenated and deoxygenated hemoglobin are equal, is at approximately 798 nm with a value of 0.0126 mm^{-1}. The absorption coefficient increases as the oxygen saturation decreases for wavelengths below the isosbestic point. Inversely, for wavelengths greater than the isosbestic point the absorption coefficient decreases with decreasing oxygen saturation. As the wavelength approaches the upper end of the tested spectrum, the contributions of the oxy- and deoxyhemoglobin begin to have less impact, with the absorption coefficient only decreasing by 6.3% at 947 nm when the oxygen saturation changes from 70% to 40%.

Generated Mesh

A 3D volumetric mesh was generated from the 3D MRI images (Figure 2). Following the addition of the four nodes corresponding with the detectors, and the subsequent re-meshing, the mesh contained 141880 nodes, 832124 elements, and 292284 surface faces. The node list is a three-column array containing the X, Y, and Z coordinates of each node. The row number of each node is the node ID. The element list contains 5 columns. The first four columns correspond with the four corners of each tetrahedral element. The values in these columns are the node IDs for that element vertex. The fifth column is the property ID for that element, determining if the tissue has the optical properties of skin, skull, CSF, or brain tissue. The face list consists of three columns

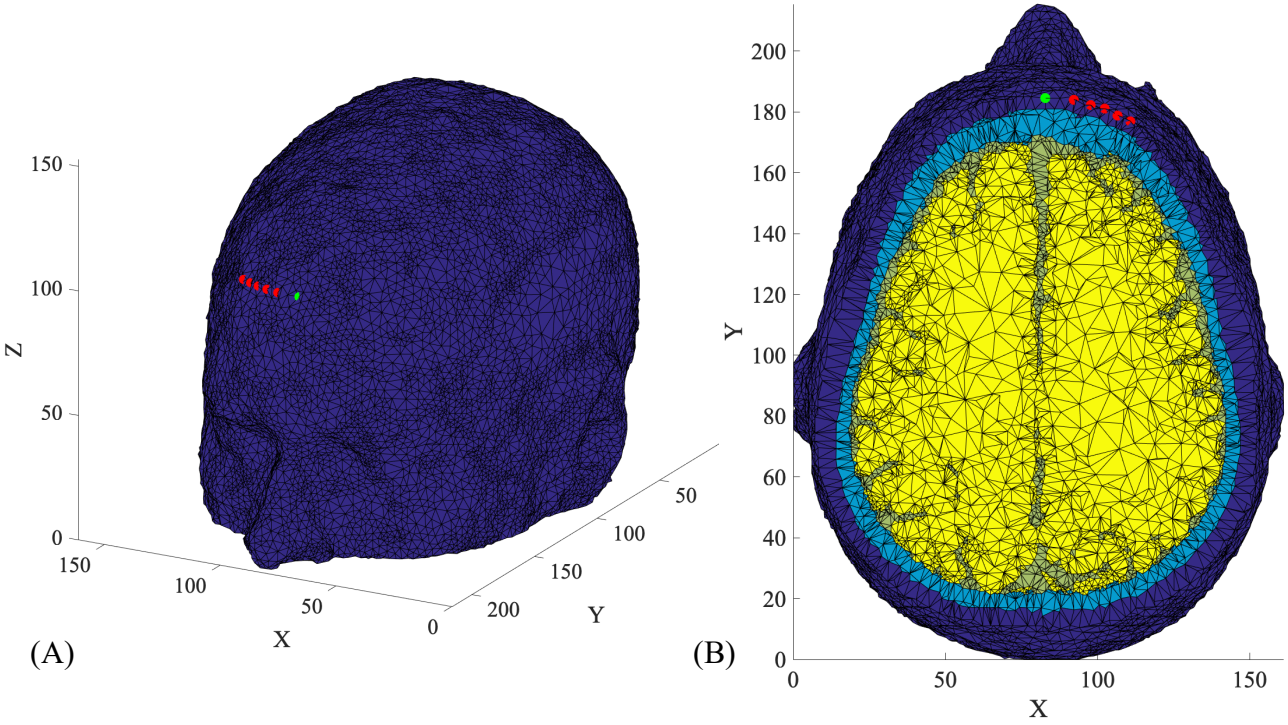

Figure 2. The volumetric mesh generated from the segmentations of the 3D MRI images. The source and detectors have been placed on the mesh to indicate their positions. The source is the green dot and the detectors are the red. All units are in mm. (A) The complete mesh with source and detectors shown. (B) A view of the X-Y plane, with the mesh truncated in the Z axis at the source-detector position to show the cross section of the head. The dark blue elements are the skin, the light blue is the bone, green is CSF, and yellow is the brain tissue.

containing the node ID for each of the vertexes, similar to the first four columns of the element list.

Photon Simulations

For each oxygen saturation level, a 298 x 10 structure with 3 fields were produced. Each row corresponds to one wavelength, ranging from 650 nm to 947 nm. Each column in the structure corresponds to a different seed number for that same wavelength. The three fields in the structure are detector output, probe position, and fluence. The detector output contains all the information about the photons which reached the detectors, including which detector registered the photon, the partial distance each photon spent in each tissue, the output weighting of the photon, the number of scattering events that occurred for each photon subdivided by the medium, and the exact location and direction of the photon when it reached the detectors. The probe positions are the locations of the source and detectors. Fluence is a 5 by 312 array, containing the fluence at each of the 5 detectors over the course of the simulations.

CW-NIRS

The total fluence for each wavelength of the varying oxygen saturations were plotted against one another for every source-detector distance. The plot for the 30 mm source-detector distance is shown in Figure 3A.

The percent difference of the saturation levels compared to the 70% brain oxygen is shown in Figure 3B for the 30 mm source-detector distance. The largest difference was consistently found at a wavelength of 696 nm, with a percent difference reaching 2.9% when the 40% oxygen saturation is compared to the 70%. The minimum difference was measured at 798 nm with only 0.004% between the 40% to 70% oxygen saturation for the 30 mm source-detector distance.

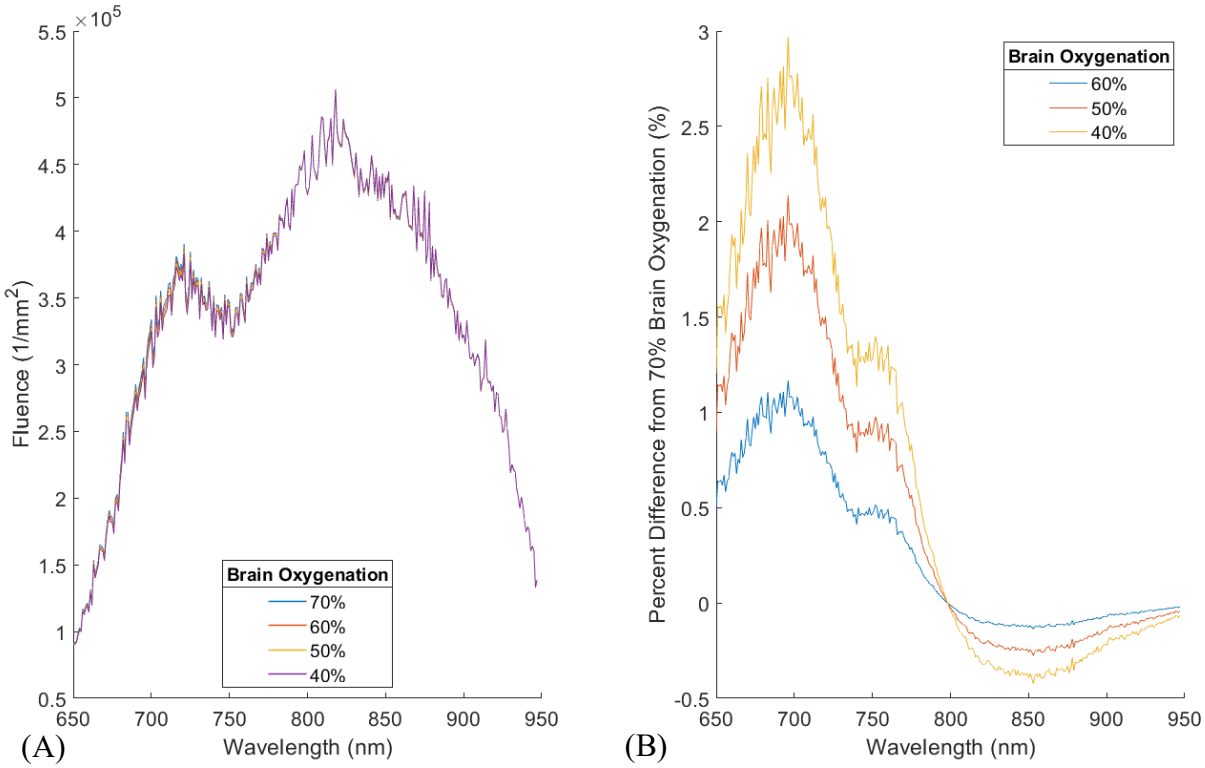

Figure 3. The total fluence for the 30 mm source-detector distance from the CW-NIRS experiments. For each wavelength, the fluence of each simulation was summed and then averaged to get a more accurate value with less noise. (A) The fluence from four different brain oxygen saturation levels for the *in silico* CW-NIRS experiments. (B) The percent difference between the 70% oxygen saturation and the other saturation levels, computed using Equation 2.

TR-NIRS

The summed fluence from 2 ns to 4 ns for each wavelength of each oxygen saturation were plotted against each other for each source-detector distance. The plot for the 30 mm source-detector distance is shown in Figure 4A.

To better visualize the difference between the oxygenation levels, the percent difference between the 70% brain oxygen saturation and the other saturation levels were compared; Figure 4B shows this plotted for the 30 mm source-detector distance. The greatest difference was consistently measured at the 657 nm wavelength, with a percent difference reaching 73.6% when the 40% oxygen saturation was compared to the 70%. The minimum difference was obtained at 798 nm, with only 0.13% difference between the 40% and the 70% oxygen saturation for the 30 mm source-detector distance.

The effective absorption coefficient of the head was retrieved from the TR-NIRS simulations. Figure 5 displays the recovered absorption coefficients for all the wavelengths and for each cerebral oxygenation level. The recovered absorption coefficients showed little change as a function of source-detector distance, with a maximum difference of 0.0025 mm^{-1} between the 10 mm and 30 mm source-detector distances. The trends found in the graph of the recovered absorption coefficient match the trends found in the inputted brain absorption coefficients (see Figures 1B and 5). Specifically, the overall shapes of the curves are similar, and the isosbestic point occurs at the same wavelength, 798 nm. Both graphs have peaks centered near 756 nm, as well as troughs centered around 726 nm and 798 nm. Both Figures 1B and 5 also show a sharp increase in absorption after 921 nm. Prior to the isosbestic point at 798nm, the absorption coefficient is lower for the higher oxygen saturations in both graphs. Conversely, the absorption coefficient increases with oxygen saturations after the isosbestic point in both graphs.

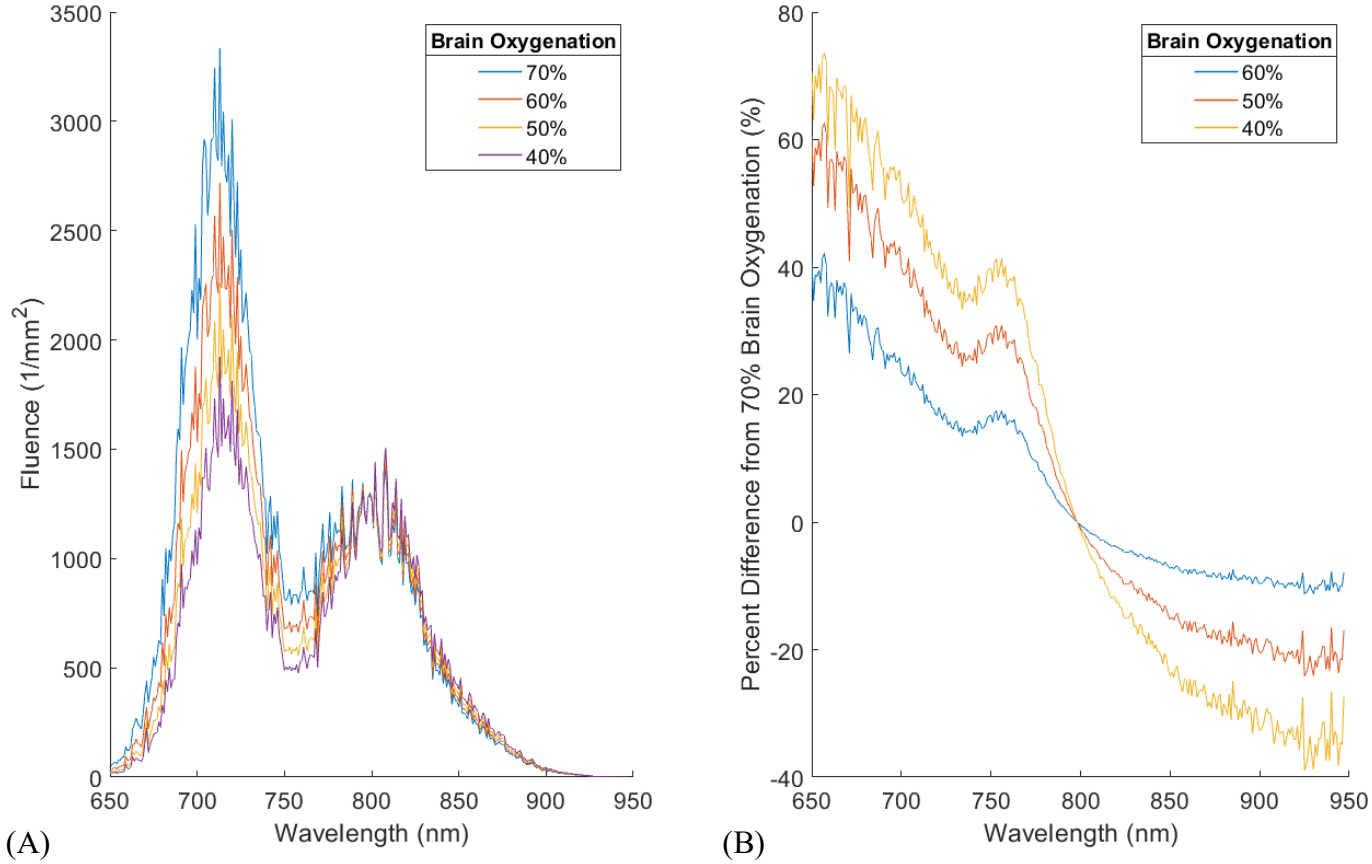

Figure 4. The total fluence from 2 ns to 4ns for the 30 mm source-detector distance, as would be measured by a TR-NIRS device. For each wavelength, the number of photons that are detected between 2ns and 4 ns was computed to isolate the late photons and reduce the noise. (A) The fluence from four different brain oxygen saturation levels compared with each other. (B) The percent difference from 70% oxygen saturation to the over saturation values. The formula used to calculate this was Equation 2.

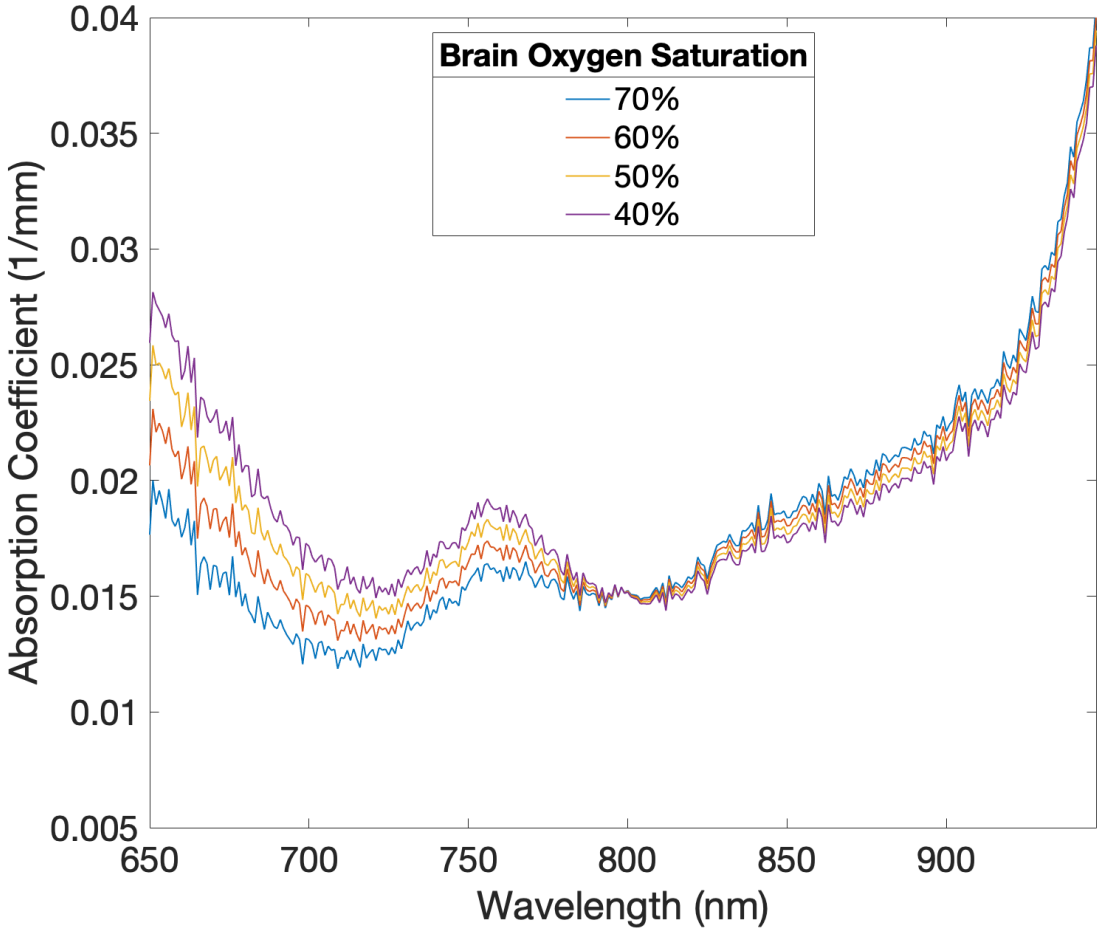

Figure 5. The recovered absorption coefficients from the TR-NIRS simulations for all the wavelengths and at the different brain oxygen saturation levels. The trends in the recovered absorption coefficient match the trends in the inputted brain absorption coefficients, seen in Figure 1B.

Discussion

Brain Absorption Coefficient

The brain absorption coefficients we computed for the 70% oxygenation are similar to the values reported in the literature (Johansson, 2010). This leads us to believe that the concentrations of each of the chromophores used in the model were accurate. Additionally, since the simulated absorption coefficient included water, oxyhemoglobin, and hemoglobin, the output absorption coefficient spectra were expected to have key features found in the absorption coefficient spectra of the individual chromophores (i.e., water, oxyhemoglobin, and hemoglobin). Specifically, deoxyhemoglobin's peak at 758 nm and troughs at 733nm and 800, oxyhemoglobin's broad peak at 925 nm, and the sharp increase in absorption of water beginning at 925 nm. The isosbestic point of oxy- and deoxyhemoglobin also appeared in the calculated brain absorption coefficient at the same location as seen in the literature which provided further validation (Jöbsis, 1977).

Generated Mesh

The generated 3D volumetric mesh closely mimicked the 3D medical MRI which was used as a guide for the segmentations. Looking at a cross-section of the head, such as in Figure 2B, it is possible to clearly see the different tissues. The tissue boundaries accurately match the tissue boundaries from the original tissue segmentations, as well as the MRI from which the segmentations were created. The volumetric mesh allowed for the simulation of photon propagation, taking into account the complex geometry of the structures which make up the human head.

The workflow established for the segmentation and mesh generation from 3D medical images is both robust and easy to execute. This workflow can be applied to any 3D medical image, allowing for the generation of 3D volumetric meshes for photon simulation for any body part.

Photon Simulations

An effective methodology for accurately assigning optical properties to the volumetric mesh and simulation of photons therein has been developed. The photon simulations take into account the complex geometry and heterogenous optical properties of the medium and allow for a fast and accurate simulation of how near-infrared light propagates in the medium. This workflow will streamline future work involving photon simulations and allow for easy control of variables.

Furthermore, we also found that running ten one million photon simulations with varying seed number before averaging the results was both faster and produced less noise than a single 10 million photon simulation. This was likely faster because the computer had to use less memory to store all the photon data, as only the photons at the detector were ultimately recorded. By running ten one million photon simulations, the photons at all the other nodes in the mesh that were not at the detector were purged every million photons, as opposed to only deleting the unneeded photon information after all 10 million photons were simulated. This resulted in significantly less computer memory being used throughout the simulation process.

It is believed that the reason there was less noise was due to the changing seed number. The seed number is responsible for the random path that the photons travel, but eventually the random numbers repeat themselves as MMC is unable to generate true random numbers. By changing the seed number, a different set of random numbers were used in the photon simulations, increasing the statistical accuracy of the Monte-Carlo simulations.

CW-NIRS

The changes in total fluence from the CW-NIRS simulations were less pronounced than expected. In previous work involving using CW-NIRS to measure cerebral oxygenation in neonates, it was shown CW-NIRS is capable of effectively monitoring cerebral oxygenation

(Tamussino *et al.*, 2016). In theory, this same method should be applicable to adults, but with decreased effectiveness. However, the maximum of a 2.9% difference between the 70% and 40% oxygenation shows that CW-NIRS would not be an effective method for monitoring brain oxygenation in adults. While the total fluence reaching the detectors is still extremely high (reaching a maximum of $5.066*10^6$ mm^{-2} at a wavelength of 818 nm), the number of photons that are interrogating the brain tissue is extremely low. This is likely due to high absorption of the skull, since the photons that reach the brain must travel through the skull twice. Supporting the idea that the skull is the reason the change is so minor in adults is that the skull tissue is much thinner in neonates (Li *et al*., 2015; Verdecchia *et al.*, 2016).

While the maximum percent difference was 3%, the vast majority of the percent differences were much smaller and would be very challenging to detect clinically for multiple reasons. Notably, there are noise fluctuations present in CW-NIRS devices which can be as large or larger than the percent differences measured across the majority of the spectrum (Kirilina *et al.*, 2013). These noise fluctuations could be misinterpreted as drops in cerebral oxygenation, leading to potential misdiagnosis and mistreatment. There are also changes in the extra-cerebral layers, such as the skin, which are larger than the changes seen here (Kirilina *et al.*, 2013). For example, increases to blood flow in the skin result in changes to the optical properties of the tissue, which could be misinterpreted as changes in cerebral oxygenation (Kirilina *et al.*, 2013). Finally, even minor changes in probe or detector positions could affect the readings of the detectors, which could once again be misinterpreted as changes in brain oxygen saturation. Due to these reasons, we do not recommend CW-NIRS for intraoperative monitoring of adult cerebral oxygen saturation.

TR-NIRS

The TR-NIRS results were a lot more promising than those of the CW-NIRS and more closely matched what we expected. Since TR-NIRS uses the TPSF of the photons instead of analysing the total intensity, it was expected to better correlate with the changes in cerebral oxygenation. Using the TPSF has the advantage of recording the fluence as a function of time, which allows for the removal of photons which are unlikely to have penetrated the brain. In order for the light to have penetrated the brain and returned to the surface, the path length of the photons would have to be much greater than the photons which only traveled through the extra-cerebral layers. The increased path length means that the photons which passed through the brain would on average arrive at the detectors later than those which did not. As such, the change in intensity of the TPSF curves would be greatest for later time points, as shown by our results.

Since TR-NIRS generates a TPSF instead of summing the intensity like in CW-NIRS, the TR-NIRS detectors need a much larger dynamic range to accurately record the intensity changes over time. The maximum total fluence of the CW-NIRS in these experiments are approximately three orders of magnitude greater than the maximum total fluence of the late photons used in TR-NIRS. Typically, TR-NIRS detectors have a dynamic range of approximately eight orders of magnitude, meaning that the method used in these experiments would be feasible *in vivo* (Hamamatsu, 2017).

The percent differences between the brain oxygen saturation levels were much more pronounced in the TR-NIRS results than they are in CW-NIRS. The maximum percent difference measured with the TR-NIRS was approximately 72.6% when the oxygen saturation drops from 70% to 40% at 657 nm, compared to a maximum change of only 3% with CW-NIRS at 696 nm. If one were to look at the 696 nm wavelength for the TR-NIRS for a direct comparison between

the two modalities at the same wavelength, TR-NIRS shows a 56% difference between the 70% and 40% oxygenation. Even a drop from 70% to 60% brain oxygen saturation resulted in a change in fluence of 26%, which is substantially higher than the 1.2% corresponding change in fluence found in the CW-NIRS simulations. These are distinctive percent differences which would not easily be confused with noise. Based on these experiments, using a multi-wavelength TR-NIRS with wavelengths at approximately 650 nm, 700 nm, 750 nm, 800 nm, 850 nm, and 900 nm, it should be possible to accurately and effectively monitor adult cerebral oxygenation. These wavelengths are recommended as they span the 1st optical window and cover many key features of the absorption spectra of water, oxyhemoglobin, and deoxyhemoglobin. This recommendation is similar to previous studies, though the suggested wavelengths vary due to different chromophores being monitored (Arifler, Zhu, Madaan & Tachtsidis, 2015).

The recovered absorption coefficient calculated from the TR-NIRS simulations follows the same trends as the inputted brain oxygen saturations. The characteristic properties of the water, oxyhemoglobin, and deoxyhemoglobin absorption spectra mentioned earlier are all present in the recovered absorption spectra. Overall, the recovered absorption coefficients are slightly higher than the inputted brain absorption coefficients. This is due to the additional absorption of the extra-cerebral layers, as the photons must pass through those tissues when entering and exiting the brain. The ability to recover the absorption coefficients works as a validation for the simulation model, as the equations used to generate the recovered absorption coefficient are the same equations used to calculate the optical properties of a tissue *in vivo* (Kienle & Patterson, 1997).

Limitations

There are a few limitations to this study. First, the absorption coefficients for the brain were calculated using only three chromophores. In the actual brain, there are many more chromophores

than just water, oxyhemoglobin, and deoxyhemoglobin, which contribute to the absorption of light in the near-infrared region. While using only the three main contributors gives an approximation of the true absorption coefficient of the brain, further studies should incorporate additional chromophores in order to provide more accurate simulations. Alternatively, the absorption coefficient could be measured directly from the brain using animal models.

Another limitation of this study is the placement of the source and detectors. As seen in Figure 2, the source was placed on the centre of the forehead with the detectors going towards the right ear. This source placement has two limitations: first, the source was placed over the thickest part of the skull, leading to increased scattering and absorption; and two the source is directed directly between the left and right hemispheres of the brain. Having the source directed between the two hemispheres is an issue as the CSF is the predominant tissue filling that region and has an extremely low scattering coefficient. It is possible that due to the low scattering coefficient many photons are traveling straight through the model and not being scattered back towards the detectors, leading to reduction in the detected signal.

A final limitation of this study is that all wavelengths and cerebral oxygenations used the same ten seed numbers. As mentioned previously, the seed numbers are used to generate the random path the simulated photons will take. It was chosen to use the same ten seed numbers in order to ensure the seed number would not introduce any additional variability. However, doing so resulted in the exact same noise occurring in each simulation. While having identical noise is unrealistic in an *in vivo* experiment, it was judged to be the best option for these simulations. By not introducing additional variability by changing the seed number, it ensured that any variances in the simulations are a direct result of the changing brain oxygen saturation.

Conclusion

We have developed a simple and robust workflow for the segmentation and mesh generation from 3D medical images such as MRIs, followed by accurate simulation of how near-infrared light propagates in those meshes, taking into account the complex and heterogeneous properties of the subject. We have also conducted an analysis of the effectiveness of both CW-NIRS and TR-NIRS for monitoring cerebral oxygenation in adults. The results show that TR-NIRS is more sensitive to changes in cerebral oxygenation in adults than CW-NIRS. While CW-NIRS is highly effective for monitoring the cerebral oxygen saturation in neonates as their skulls are thin, it is likely that the extra-cerebral layers of the mature skull are too thick to make this a viable method in adults. Since TR-NIRS is capable of excluding the early photons, it is much less susceptible to the photons which only traveled through the extra-cerebral tissues than CW-NIRS. These simulations suggest that TR-NIRS would be the most appropriate method for monitoring cerebral oxygen saturation in adult patients. Future work should include running further simulations with the source and detectors placed on the temple in order to verify if this would make a difference in the amount of signal received, as well as randomly generating new seed numbers for each simulation in order to allow the noise to behave as it does *in vivo*, as this would give a closer approximation to the output of true CW-NIRS and TR-NIRS devices. Finally, future work should involve *in vivo* experiments using a multi-wavelength TR-NIRS in order to monitor cerebral oxygenation in animal models of the adult head (e.g., adult pig) to further validate the findings of this study. Such an approach has potential uses in adult cardiac surgery and trauma patients, as well as for bedside monitoring of brain oxygenation in patients with a high risk of stroke in the intensive care unit.

Acknowledgements

I would like to thank Dr. Mamadou Diop for all of the help he has provided me throughout my thesis project and my undergraduate career. His aid and guidance have been invaluable to me. I would also like to thank Laura Mawdsley and Seva Ioussoufovitch for their time and assistance throughout my research.

Additionally, I would like to acknowledge and thank my sources of funding, Western University, Schulich School of Medicine and Dentistry, Lawson Research Institute, and the Natural Sciences and Engineering Research Council of Canada (NSERC) for providing me the opportunity to complete this research.

References

3D Slicer. (2019). Retrieved January 25, 2019, from https://www.slicer.org/

Arifler, D., Zhu, T., Madaan, S., & Tachtsidis, I. (2015). Optimal wavelength combinations for near-infrared spectroscopic monitoring of changes in brain tissue hemoglobin and cytochrome c oxidase concentrations. *Biomedical Optics Express*, *6*(3), 933–947. https://doi.org/10.1364/BOE.6.000933

Auger, H., Bherer, L., Boucher, É., Hoge, R., Lesage, F., & Dehaes, M. (2016). Quantification of extra-cerebral and cerebral hemoglobin concentrations during physical exercise using time-domain near infrared spectroscopy. *Biomedical Optics Express*, *7*(10), 3826–3842. https://doi.org/10.1364/BOE.7.003826

Chen, J., Fang, Q., & Intes, X. (2012). Mesh-based Monte Carlo method in time-domain widefield fluorescence molecular tomography. *Journal of Biomedical Optics*, *17*(10), 106009. https://doi.org/10.1117/1.JBO.17.10.106009

Diop, M., Elliott, J. T., Tichauer, K. M., Lee, T.-Y., & St. Lawrence, K. (2009). A broadband continuous-wave multichannel near-infrared system for measuring regional cerebral blood flow and oxygen consumption in newborn piglets. *Review of Scientific Instruments*, *80*(5), 054302. https://doi.org/10.1063/1.3123347

Fedorov, A., Beichel, R., Kalpathy-Cramer, J., Finet, J., Fillion-Robin, J.-C., Pujol, S., … Kikinis, R. (2012). 3D Slicer as an Image Computing Platform for the Quantitative Imaging Network. *Magnetic Resonance Imaging*, *30*(9), 1323–1341. https://doi.org/10.1016/j.mri.2012.05.001

Gering, D. T., Nabavi, A., Kikinis, R., Hata, N., O'Donnell, L. J., Grimson, W. E. L., … Wells, W. M. (2001). An integrated visualization system for surgical planning and guidance using

image fusion and an open MR. *Journal of Magnetic Resonance Imaging*, *13*(6), 967–975. https://doi.org/10.1002/jmri.1139

Grogan, K., Stearns, J., & Hogue, C. W. (2008). Brain Protection in Cardiac Surgery. *Anesthesiology Clinics*, *26*(3), 521–538. https://doi.org/10.1016/j.anclin.2008.03.003

Jacques, S. L. (2013). Optical properties of biological tissues: a review. *Physics in Medicine and Biology*, *58*(11), R37–R61. https://doi.org/10.1088/0031-9155/58/11/R37

Jöbsis, F. F. (1977). Noninvasive, Infrared Monitoring of Cerebral and Myocardial Oxygen Sufficiency and Circulatory Parameters. *Science*, *198*(4323), 1264–1267.

Johansson, J. D. (2010). Spectroscopic method for determination of the absorption coefficient in brain tissue. *Journal of Biomedical Optics*, *15*(5), 057005. https://doi.org/10.1117/1.3495719

Kienle, A., & Patterson, M. S. (1997). Improved solutions of the steady-state and the time-resolved diffusion equations for reflectance from a semi-infinite turbid medium. *JOSA A*, *14*(1), 246–254. https://doi.org/10.1364/JOSAA.14.000246

Kikinis, R., Pieper, S. D., & Vosburgh, K. G. (2014). 3D Slicer: A Platform for Subject-Specific Image Analysis, Visualization, and Clinical Support. In F. A. Jolesz (Ed.), *Intraoperative Imaging and Image-Guided Therapy* (pp. 277–289). New York, NY: Springer New York. https://doi.org/10.1007/978-1-4614-7657-3_19

Kirilina, E., Yu, N., Jelzow, A., Wabnitz, H., Jacobs, A. M., & Tachtsidis, I. (2013). Identifying and quantifying main components of physiological noise in functional near infrared spectroscopy on the prefrontal cortex. *Frontiers in Human Neuroscience*, *7*. https://doi.org/10.3389/fnhum.2013.00864

Kowalczyk, A. K., Bachar, B. J., & Liu, H. (2016). Neuromonitoring during adult cardiac surgery. *Journal of Biomedical Research*, *30*(3), 171–173. https://doi.org/10.7555/JBR.30.20150159

Li, Z., Park, B.-K., Liu, W., Zhang, J., Reed, M. P., Rupp, J. D., … Hu, J. (2015). A Statistical Skull Geometry Model for Children 0-3 Years Old. *PLoS ONE, 10(5)*. https://doi.org/10.1371/journal.pone.0127322

Machida, M. (2017). The time-fractional radiative transport equation—Continuous-time random walk, diffusion approximation, and Legendre-polynomial expansion. *Journal of Mathematical Physics*, *58*(1), 013301. https://doi.org/10.1063/1.4973441

MATLAB and Image Processing Toolbox. (n.d.). (Version 2018b). Natick, Massachusetts, United States: The MathWorks, Inc.

Oddo, M., & Bösel, J. (2014). Monitoring of Brain and Systemic Oxygenation in Neurocritical Care Patients. *Neurocritical Care*, *21*, 103–120. https://doi.org/10.1007/s12028-014-0024-6

Photomultiplier tubes and assemblies for scintillation counting and high energy physics. (2017, April). Hamamatsu Photonics. Retrieved from https://www.hamamatsu.com/resources/pdf/etd/High_energy_PMT_TPMZ0003E.pdf

Pieper, S., Halle, M., & Kikinis, R. (2004). 3D Slicer. In *2004 2nd IEEE International Symposium on Biomedical Imaging: Nano to Macro (IEEE Cat No. 04EX821)* (pp. 632-635 Vol. 1). https://doi.org/10.1109/ISBI.2004.1398617

Pieper, S., Lorensen, B., Schroeder, W., & Kikinis, R. (2006). The NA-MIC Kit: ITK, VTK, pipelines, grids and 3D slicer as an open platform for the medical image computing

community. In *3rd IEEE International Symposium on Biomedical Imaging: Nano to Macro, 2006.* (pp. 698–701). https://doi.org/10.1109/ISBI.2006.1625012

Qianqian Fang, & Boas, D. A. (2009). Tetrahedral mesh generation from volumetric binary and grayscale images. *2009 IEEE International Symposium on Biomedical Imaging: From Nano to Macro*, 1142–1145. https://doi.org/10.1109/ISBI.2009.5193259

Shi, L., Sordillo, L. A., Rodríguez-Contreras, A., & Alfano, R. (2016). Transmission in near-infrared optical windows for deep brain imaging. *Journal of Biophotonics*, *9*(1–2), 38–43. https://doi.org/10.1002/jbio.201500192

Sood, B. G., McLaughlin, K., & Cortez, J. (2015). Near-infrared spectroscopy: applications in neonates. *Seminars in Fetal & Neonatal Medicine*, *20*(3), 164–172. https://doi.org/10.1016/j.siny.2015.03.008

Sun, X., Lindsay, J., Monsein, L. H., Hill, P. C., & Corso, P. J. (2012). Silent Brain Injury After Cardiac Surgery: A Review: Cognitive Dysfunction and Magnetic Resonance Imaging Diffusion-Weighted Imaging Findings. *Journal of the American College of Cardiology*, *60*(9), 791–797. https://doi.org/10.1016/j.jacc.2012.02.079

Taddeucci, A., Martelli, F., Barilli, M., Ferrari, M., & Zaccanti, G. (1996). Optical properties of brain tissue. *Journal of Biomedical Optics*, *1*(1), 117–124. https://doi.org/10.1117/12.227816

Tamussino, A., Urlesberger, B., Baik, N., Schwaberger, B., Binder-Heschl, C., Schmölzer, G. M., … Pichler, G. (2016). Low cerebral activity and cerebral oxygenation during immediate transition in term neonates—A prospective observational study. *Resuscitation*, *103*, 49–53. https://doi.org/10.1016/j.resuscitation.2016.03.011

Verdecchia, K., Diop, M., Lee, A., Morrison, L. B., Lee, T.-Y., & St. Lawrence, K. (2016). Assessment of a multi-layered diffuse correlation spectroscopy method for monitoring cerebral blood flow in adults. *Biomedical Optics Express*, *7*(9), 3659–3674. https://doi.org/10.1364/BOE.7.003659